Article

Vulnerability of Antarctica's ice shelves to meltwater-driven fracture

https://doi.org/10.1038/s41586-020-2627-8

Received: 28 August 2019

Accepted: 29 June 2020

Published online: 26 August 2020

Check for updates

Ching-Yao Lai[1]✉, Jonathan Kingslake[1,2], Martin G. Wearing[3], Po-Hsuan Cameron Chen[4], Pierre Gentine[5], Harold Li[6], Julian J. Spergel[1,2] & J. Melchior van Wessem[7]

Atmospheric warming threatens to accelerate the retreat of the Antarctic Ice Sheet by increasing surface melting and facilitating 'hydrofracturing'[1–7], where meltwater flows into and enlarges fractures, potentially triggering ice-shelf collapse[3–5,8–10]. The collapse of ice shelves that buttress[11–13] the ice sheet accelerates ice flow and sea-level rise[14–16]. However, we do not know if and how much of the buttressing regions of Antarctica's ice shelves are vulnerable to hydrofracture if inundated with water. Here we provide two lines of evidence suggesting that many buttressing regions are vulnerable. First, we trained a deep convolutional neural network (DCNN) to map the surface expressions of fractures in satellite imagery across all Antarctic ice shelves. Second, we developed a stability diagram of fractures based on linear elastic fracture mechanics to predict where basal and dry surface fractures form under current stress conditions. We find close agreement between the theoretical prediction and the DCNN-mapped fractures, despite limitations associated with detecting fractures in satellite imagery. Finally, we used linear elastic fracture mechanics theory to predict where surface fractures would become unstable if filled with water. Many regions regularly inundated with meltwater today are resilient to hydrofracture—stresses are low enough that all water-filled fractures are stable. Conversely, 60 ± 10 per cent of ice shelves (by area) both buttress upstream ice and are vulnerable to hydrofracture if inundated with water. The DCNN map confirms the presence of fractures in these buttressing regions. Increased surface melting[17] could trigger hydrofracturing if it leads to water inundating the widespread vulnerable regions we identify. These regions are where atmospheric warming may have the largest impact on ice-sheet mass balance.

Where ice shelves—the floating extensions of ice sheets—are laterally confined, they generate resistive stress and transmit this upstream to slow the flow of ice into the ocean. This is called buttressing. Areas with larger tensile resistive stresses[2,18] provide less buttressing[13,19]. When buttressing ice shelves collapse, upstream glaciers accelerate[14–16]. Observations and models have linked ice-shelf collapse to surface melting[4,5,8,10,20] through hydrofracturing; where meltwater flows into surface fractures, imposing additional loading and driving unstable fracture growth[1,2]. Repeated hydrofracturing close to an ice-shelf edge has been hypothesized as a potential mechanism driving collapse[4]. Flexural stresses generated by the filling and draining of lakes on ice shelves may also facilitate hydrofracturing and trigger collapse[5,21,22]. Although hydrofracturing has so far only been included in ice-sheet models with simple parameterizations[9,10], simulations predict that it could accelerate the retreat of the Antarctic Ice Sheet in response to atmospheric warming[9,10].

Antarctica's response to surface melting

Hydrofracturing requires sufficient surface meltwater and tensile stress within the ice shelves. However, not all parts of ice shelves provide substantial buttressing and thus, to predict the impact of atmospheric warming on Antarctic ice loss, we must predict (1) the distribution of meltwater on ice shelves[7,17,23–25]; (2) the regions of ice shelves providing buttressing[13,19]; and (3) the regions of ice shelves that will undergo hydrofracturing if meltwater accumulates (Fig. 1; ref. [26]). Progress has been made in constraining where meltwater accumulates today and will in the future (the upper circle in Fig. 1). Stokes et al.[25] comprehensively mapped lakes in East Antarctica using satellite imagery from January 2017. Trusel et al.[17] predicted that melt rates seen in areas that have undergone catastrophic collapse in the past will become widespread this century. Alley et al.[7] assessed the state of firn on ice shelves, which is linked to the ability of an ice shelf to retain surface water[27], using microwave backscatter observations. They found some locations already in a state that would allow lake formation and potentially hydrofracturing[7,27]. However, a location will only undergo hydrofracturing if local stresses allow, with higher tensile stress promoting hydrofracturing. For clarity, here we will refer to the tendency of a location to hydrofracture if inundated with water as its vulnerability to hydrofracture. Crucially, areas of higher tensile stress[2] provide less buttressing[13,19], yet are most

[1]Lamont-Doherty Earth Observatory, Columbia University, Palisades, NY, USA. [2]Department of Earth and Environmental Sciences, Columbia University, New York, NY, USA. [3]School of Geosciences, University of Edinburgh, Edinburgh, UK. [4]Google, Mountain View, CA, USA. [5]Department of Earth and Environmental Engineering, Columbia University, New York, NY, USA. [6]Department of Computer Science, Columbia University, New York, NY, USA. [7]Institute for Marine and Atmospheric Research Utrecht, Utrecht University, Utrecht, The Netherlands. ✉e-mail: cylai@ldeo.columbia.edu

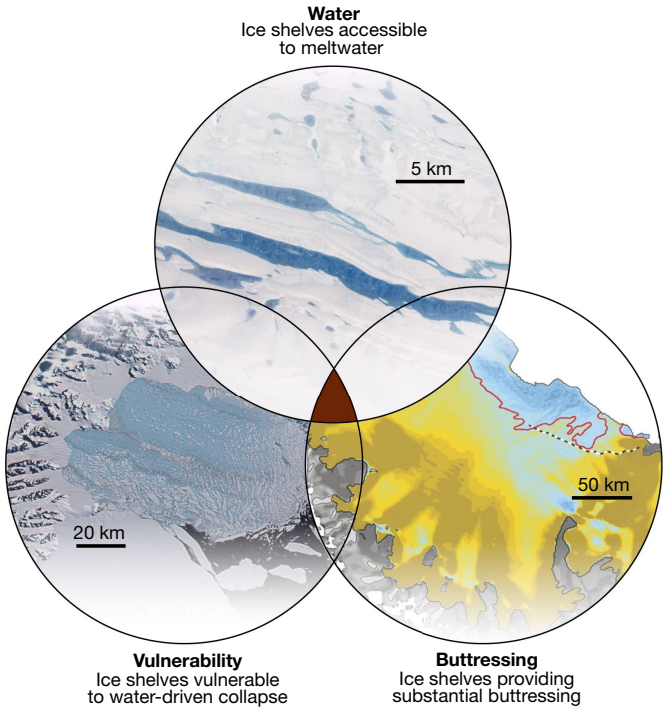

Fig. 1 | Conceptualizing the regions of Antarctic ice shelves that will control the ice sheet's response to atmospheric warming. Circles represent ice-shelf regions (top) where meltwater accumulates, (bottom left) that are vulnerable to hydrofracture if covered in meltwater, and (bottom right) where substantial buttressing is generated. Images show: Amery Ice Shelf with water accumulated in large melt ponds, 21 February 1989, Landsat 4, NASA (top); the collapse of Larsen B Ice Shelf, 7 March 2002, MODIS, NASA (bottom left); modelled estimate of buttressing on Larsen C Ice Shelf[13] (bottom right; reproduced from figure 3 of ref. [13] (Springer Nature)). Regions downstream of the red contour (blue) are relatively unimportant for buttressing.

vulnerable to hydrofracture. Therefore, an important open question is: are any of the regions generating substantial buttressing also vulnerable to hydrofracture under present-day conditions? Do the two lower circles in Fig. 1 overlap? This is the focus of this article.

Fracture detection with a neural network

Fracture-like features are visible in satellite imagery (for example, the 125-m-resolution MODIS mosaic of Antarctica, MOA 2009[28]), but comprehensive manual mapping is impractical (ice shelves cover 1.5 million pixels in MOA). We therefore used a deep convolutional neural network (DCNN), the U-Net[29], to identify the fracture-like features in the relatively low-resolution, but continent-wide, MOA imagery. We trained the DCNN with a subset of MOA imagery in which fracture features were manually labelled (Extended Data Fig. 1c). The output of the DCNN is a map of the likelihood (ranging from 0 to 1) that a pixel contains part of a fracture. The trained DCNN performs well when evaluated against an unseen subset of imagery (Extended Data Fig. 2). We applied the trained DCNN to map fracture-like features across all of Antarctica's ice shelves (Fig. 2). Examples of the imagery and the fracture features identified by the DCNN are shown in Fig. 3a, b, respectively. Because there are morphological similarities between surface fractures, full-thickness rifts and surface expressions of basal fractures[30–32], it is likely that they all make up a proportion of the fractures mapped by the DCNN. We refer to them throughout as fractures, but consider this limitation when comparing the DCNN results to the theoretical predictions below.

Fracture stability diagram

Next, we developed a new theoretical framework to predict the location of dry surface fractures. There are two widely adopted models for ice fracturing: the zero-stress approximation[33] and linear elastic fracture mechanics (LEFM)[2,34]. The zero-stress approximation only applies where fractures are densely spaced (fracture spacing is much smaller than fracture depth)[35]. Because the spacing between dry fractures (~1 km) is often larger than the fracture depth, we applied LEFM. Although dry-fracture depths predicted by LEFM are simply a factor of π/2 larger than those predicted by the zero-stress approximation[1] (Extended Data Fig. 5b), LEFM provides an estimate of the critical tensile resistive stress required to form dry fractures, which is crucial for this study.

To quantify how ice-shelf stress affects fracture stability, we constructed a fracture stability diagram (Fig. 3c). Vertical propagation of a stable fracture stops when it is too energetically costly to break the ice further. By contrast, unstable fractures propagate through the entire ice thickness. Fractures may form on both the surface and base of ice shelves; their stability depends on the tensile resistive stress R_{xx} (refs. [2,34]) perpendicular to the fracture, ice thickness H, fracture toughness K_{Ic} (a measurable material property)[36] and ice density ρ_i. The stability of both surface and basal fractures depends on two fundamental parameters (Supplementary Section 3), the dimensionless tensile resistive stress ($\tilde{R}_{xx}$) and dimensionless fracture toughness ($\tilde{K}_{Ic}$):

$$\tilde{R}_{xx} \equiv \frac{R_{xx}}{\rho_i g H}, \ \tilde{K}_{Ic} \equiv \frac{K_{Ic}}{\rho_i g H^{3/2}}. \quad (1)$$

We analytically derived a power law (Supplementary Section 3) for the critical tensile resistive stress R^*_{xx} that allows the formation of stable surface fractures (red curve in Fig. 3c),

$$\tilde{K}_{Ic} = \alpha(\tilde{R}^*_{xx})^{3/2}, \alpha \equiv \frac{\pi}{3}\sqrt{\frac{2}{3}}\frac{F^{3/2}}{f^{1/2}}, \quad (2)$$

where $F \approx 1.122$, $f \approx 1.068$ and α is a dimensionless pre-factor (Supplementary Section 3). This analytical expression (equation (2)) closely matches the corresponding numerical solution (black solid curve in Fig. 3c; Supplementary Section 3). When $R_{xx} < R^*_{xx}$, no surface fractures can exist according to LEFM (white area in Fig. 3c). When $\tilde{R}_{xx}$ exceeds a threshold (black dashed line in Fig. 3c), surface fractures are unstable. The transition boundaries (between no fracture, stable fracture and unstable fracture) for basal fractures with the inclusion of the effects of vertically varying temperature (Supplementary Section 7) are shown by light blue curves in Fig. 3c. In the absence of meltwater, LEFM predicts that a basal fracture will destabilize at a smaller $\tilde{R}_{xx}$ than a surface fracture.

To assess where the DCNN-identified fracture features lie in this space, we computed $\tilde{R}_{xx}$ and $\tilde{K}_{Ic}$ for every fracture location (at 1 km resolution) using observed H (ref. [37]), $K_{Ic} = 150$ kPa m$^{1/2}$ (from laboratory measurements)[36], strain rates derived from a data-constrained flow model[13] and ice viscosity calculated using ice surface temperature from a regional climate model[38] (Extended Data Fig. 6c). Fig. 3c plots them on the parameter space as a density map. Most fracture features (89% of 31,962 locations identified as fractures by the DCNN shown in Fig. 3c) lie in the parameter region where the theory predicts stable surface fractures (grey area in Fig. 3c). We also note that 56% of the 31,962 identified fracture features lie in the parameter regime of stable basal fractures. Given the simplicity of the theory and the limitations of the DCNN mapping, this agreement is encouraging and suggests that the theory predicts both stable surface and basal fractures across realistic ranges of $\tilde{R}_{xx}$ and $\tilde{K}_{Ic}$. Note that no parameters were tuned to determine the locations of data on Fig. 3c.

Vulnerability to unstable hydrofracture

To estimate vulnerability to hydrofracture across all ice shelves, we next examined the extreme case when water inundates all ice shelves. In this way, we estimated the geographic extent of the lower-left circle in Fig. 1. When surface fractures are filled with meltwater, the weight

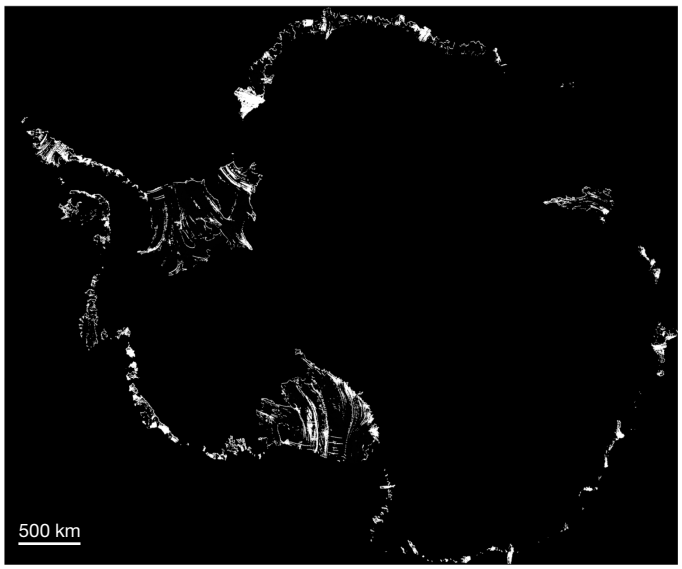

Fig. 2 | Continent-wide fracture map. Locations of fracture features classified by the DCNN are marked in white. The model with the optimal performance on the validation set was chosen to generate the fracture map. The area under the receiver operating characteristics curve of the U-Net on an unseen testing set is 0.97 (Methods).

of water can destabilize the fractures, leading to unstoppable fracture propagation. However, when the ice stresses are sufficiently compressive, pre-existing water-filled fractures remain stable (Supplementary Section 5). Here we assume that surface water flows rapidly into surface fractures and does not refreeze fast enough to affect fracture propagation. Slow inflow and refreezing could stabilize surface fractures. A fracture model coupled to a hydrological model could account for this[39].

In regions where $R_{xx} > R^*_{xx}$ (red in Fig. 4a), surface fractures will be unstable if filled with water—these locations are vulnerable to hydrofracture. Where $R_{xx} < R^*_{xx}$, water-filled fractures will be stable, unless the original dry fracture is deeper than d_i (Fig. 4a). The pre-existing surface fracture depth d_i required to destabilize hydrofracture increases as R_{xx} decreases, as plotted in Extended Data Fig. 5c, d. Given that pre-existing fractures in regions of low R_{xx} are unlikely to be 50–150 m deep, we consider the ice-shelf regions marked yellow and green in Fig. 3 to be resilient to meltwater-driven fracturing. Finally, some regions have sufficiently compressive stresses that water-filled fractures cannot grow, regardless of their size (black regions in Fig. 4a).

Vulnerable and buttressing regions

Our key question is whether regions vulnerable to hydrofracture coincide with buttressing regions (Fig. 1). Both the DCNN-mapped fractures and LEFM theory suggest that they do coincide. Blue areas in Fig. 4a were identified by Fürst et al.[13] as regions of 'passive ice' that provide little buttressing. Red regions in Fig. 4 are where the ice shelf is vulnerable to hydrofracture according to our LEFM analysis and also provides substantial buttressing[13]; that is, they lie outside the passive regions recognized by Fürst et al. These regions cover 60 ± 10% of the total area of Antarctica's ice shelves. The details of the extent of these regions depend on the buttressing computation[13] and the method used to compute stresses, but the finding that buttressing and vulnerable regions substantially overlap does not (Extended Data Fig. 8). The DCNN map confirms widespread surface fractures in these regions (Fig. 2).

It does not impact our key conclusions, but we neglected the impact of the low-density, low-viscosity, near-surface firn layer and ice softening due to damage (Methods). The net effect of the firn is to slightly increase surface fracture depths (Supplementary Section 2 and Extended Data Fig. 3c) and therefore slightly increase the extent of the vulnerable regions. Conversely, damaged ice would generate lower tensile resistive stress and decrease the extent of vulnerable regions slightly (see Methods and Extended Data Fig. 8b).

Hydrofracturing can only occur if the ice-shelf surface is inundated with meltwater. Large meltwater ponds have persisted in numerous locations for decades. Many of these, for example on the George VI (Fig. 4c), Amery (Fig. 4e) and Roi Baudoin ice shelves[23,40], lie in regions that, due to low tensile (and in places compressive) resistive stresses, are resilient to hydrofracture (Fig. 4b, d). Moreover, using a recent survey of East Antarctic supraglacial lakes[25], we estimated an upper bound of only 0.6% of East Antarctic ice shelves (by area) currently provide buttressing, experience meltwater ponding and are vulnerable to hydrofracture (see Methods section 'Lake locations' and Extended Data Fig. 10). Increased meltwater ponding in resilient locations will not lead to widespread hydrofracturing according to our analysis. However,

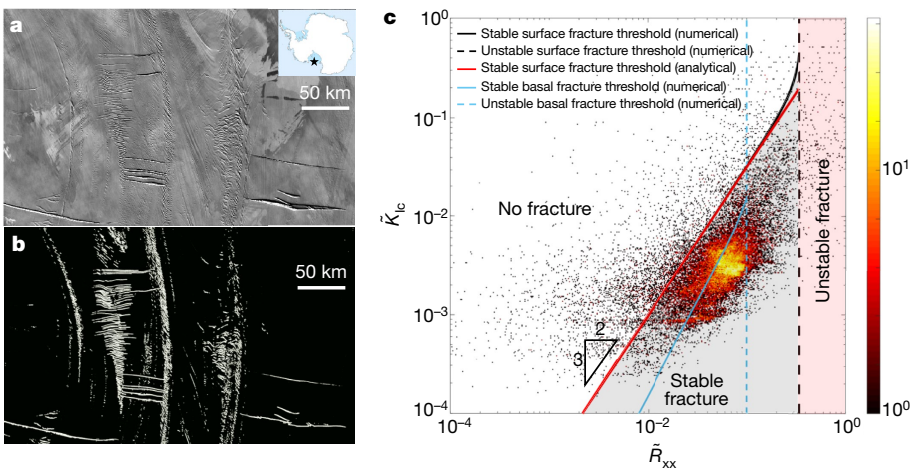

Fig. 3 | Model–observation comparison of fracture locations. a, **b**, 125-m-resolution MOA showing part of the Ross Ice Shelf (location shown by the star in the inset map) (**a**) and the fracture features (marked in white) identified by the DCNN (**b**). **c**, Stability diagram for dry surface fractures and basal fractures; $\tilde{R}_{xx}$ against $\tilde{K}_{Ic}$. The boundary between the no-fracture and stable-fracture regions was obtained numerically (black and blue curves for surface and basal fractures, respectively) and analytically (red curve for surface fractures, equation (2)). Dashed lines denote the boundary between stable and unstable fractures. $\tilde{R}_{xx}$ and $\tilde{K}_{Ic}$ (equation (1)) were computed for every fracture location detected by the DCNN and displayed as a density plot (31,962 data points); the colour bar denotes the number of fracture locations that have the same dimensionless values (Methods).

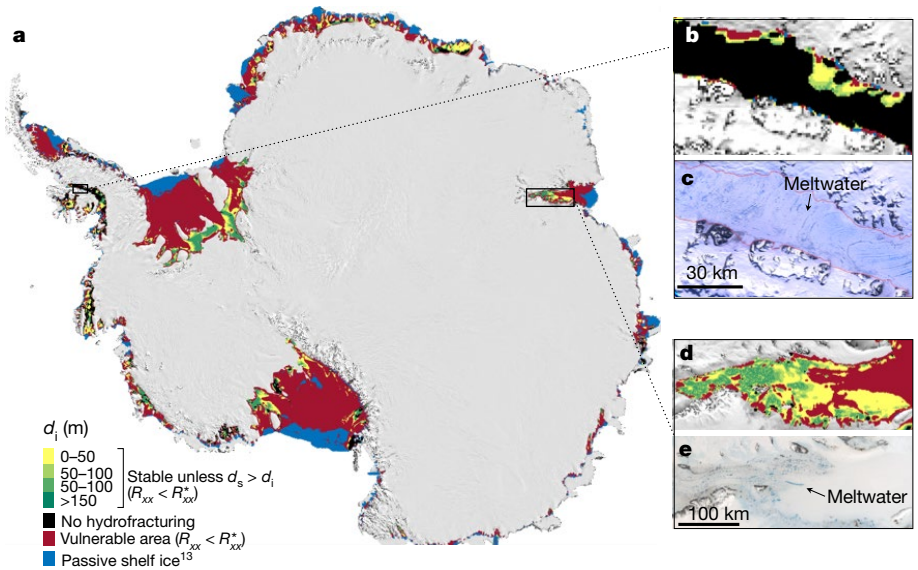

Fig. 4 | Map of ice-shelf vulnerability to hydrofracture. a, Water-filled fractures are unstable in vulnerable areas (red and blue) and stable in resilient regions (yellow and green) unless pre-existing surface fractures of depth d_i exist. Where stresses are sufficiently compressive, water-filled fractures cannot open (black). **c**, **e**, Present-day meltwater on the George VI (**c**; 4 February 1991, Landsat 5) and Amery (**e**; 15 and 17 January 2019, Landsat 8) ice shelves predominantly lies in regions resilient to hydrofracture (yellow, green and black in **b** and **d**). Blue denotes regions providing weak buttressing[13]. We find that 60 ± 10% of the Antarctic Ice Shelf area provides buttressing and is vulnerable to hydrofracture (red).

predictions of future melt[17,41] suggest that melt rates seen in locations that experience meltwater ponding today could become widespread by 2100 under high-emissions scenarios. This, coupled with present-day widespread low-porosity firn[7] and large-scale surface-meltwater drainage that can transport water long distances from melt zones[26], strongly indicates that meltwater ponding could spread to many of the buttressing and vulnerable regions under future warming scenarios.

Summary

We have used fracture mechanics, machine learning and continent-wide datasets to estimate the vulnerability of Antarctica's ice shelves to hydrofracture. Although hydrofracturing and buttressing are favoured by different stress conditions, a large proportion of Antarctic ice shelves are both vulnerable to hydrofracture, if inundated with meltwater, and provide substantial buttressing. We used a neural network to produce a continent-wide map of fracture features (Fig. 2). Our analysis yielded a fracture stability diagram based on LEFM that shows promising agreement with the fracture locations, but could be extended to include viscous[35] and thermal effects[39]. This theory could be implemented into an ice-sheet model to improve sea-level predictions and the machine learning approach to mapping fractures can easily be applied to higher-resolution imagery. If warming allows meltwater to enter the vulnerable buttressing regions we have identified, hydrofracture-driven ice-shelf collapse is possible, which could have major consequences for Antarctic mass loss and global sea-level rise.

Online content

Any methods, additional references, Nature Research reporting summaries, source data, extended data, supplementary information, acknowledgements, peer review information; details of author contributions and competing interests; and statements of data and code availability are available at https://doi.org/10.1038/s41586-020-2627-8.

1. Weertman, J. Can a water-filled crevasse reach the bottom surface of a glacier? In *Symposium on the Hydrology of Glaciers: Cambridge, 7–13 September 1969*. Publication no. 95, 139–145 (International Association of Scientific Hydrology, 1973).
2. van der Veen, C. J. Fracture mechanics approach to penetration of surface crevasses on glaciers. *Cold Reg. Sci. Technol.* **27**, 31–47 (1998).
3. Benn, D. I., Warren, C. R. & Mottram, R. H. Calving processes and the dynamics of calving glaciers. *Earth Sci. Rev.* **82**, 143–179 (2007).
4. Scambos, T. et al. Ice-shelf disintegration by plate bending and hydro-fracture: satellite observations and model results of the 2008 Wilkins Ice Shelf break-ups. *Earth Planet. Sci. Lett.* **280**, 51–60 (2009).
5. Banwell, A. F., MacAyeal, D. R. & Sergienko, O. V. Breakup of the Larsen B Ice Shelf triggered by chain reaction drainage of supraglacial lakes. *Geophys. Res. Lett.* **40**, 5872–5876 (2013).
6. Jiménez, S. & Duddu, R. On the evaluation of the stress intensity factor in calving models using linear elastic fracture mechanics. *J. Glaciol.* **64**, 759–770 (2018).
7. Alley, K. E., Scambos, T. A., Miller, J. Z., Long, D. G. & MacFerrin, M. Quantifying vulnerability of Antarctic ice shelves to hydrofracture using microwave scattering properties. *Remote Sens. Environ.* **210**, 297–306 (2018).
8. Rack, W. & Rott, H. Pattern of retreat and disintegration of the Larsen B Ice Shelf, Antarctic Peninsula. *Ann. Glaciol.* **39**, 505–510 (2004).
9. Pollard, D., DeConto, R. M. & Alley, R. B. Potential Antarctic Ice Sheet retreat driven by hydrofracturing and ice cliff failure. *Earth Planet. Sci. Lett.* **412**, 112–121 (2015).
10. DeConto, R. M. & Pollard, D. Contribution of Antarctica to past and future sea-level rise. *Nature* **531**, 591–597 (2016).
11. Schoof, C. Ice sheet grounding line dynamics: steady states, stability, and hysteresis. *J. Geophys. Res. Earth Surf.* **112**, F03S28 (2007).
12. Gudmundsson, G. H. Ice-shelf buttressing and the stability of marine ice sheets. *Cryosphere* **7**, 647–655 (2013).
13. Fürst, J. J. et al. The safety band of Antarctic ice shelves. *Nat. Clim. Change* **6**, 479–482 (2016).
14. Rignot, E. Accelerated ice discharge from the Antarctic Peninsula following the collapse of Larsen B Ice Shelf. *Geophys. Res. Lett.* **31**, L18401 (2004).
15. Scambos, T. A. Glacier acceleration and thinning after ice shelf collapse in the Larsen B embayment, Antarctica. *Geophys. Res. Lett.* **31**, L18402 (2004).
16. Wuite, J. et al. Evolution of surface velocities and ice discharge of Larsen B outlet glaciers from 1995 to 2013. *Cryosphere* **9**, 957–969 (2015).
17. Trusel, L. D. et al. Divergent trajectories of Antarctic surface melt under two twenty-first-century climate scenarios. *Nat. Geosci.* **8**, 927–932 (2015).
18. Van Der Veen, C. J. & Whillans, I. M. Force budget: I. Theory and numerical methods. *J. Glaciol.* **35**, 53–60 (1989).
19. Reese, R., Gudmundsson, G. H., Levermann, A. & Winkelmann, R. The far reach of ice-shelf thinning in Antarctica. *Nat. Clim. Change* **8**, 53–57 (2018).
20. Robel, A. A. & Banwell, A. F. A speed limit on ice shelf collapse through hydrofracture. *Geophys. Res. Lett.* **46**, 12092–12100 (2019).
21. MacAyeal, D. R., Sergienko, O. V. & Banwell, A. F. A model of viscoelastic ice-shelf flexure. *J. Glaciol.* **61**, 635–645 (2015).
22. Banwell, A. F., Willis, I. C., Macdonald, G. J., Goodsell, B. & MacAyeal, D. R. Direct measurements of ice-shelf flexure caused by surface meltwater ponding and drainage. *Nat. Commun.* **10**, 730 (2019).
23. Kingslake, J., Ely, J. C., Das, I. & Bell, R. E. Widespread movement of meltwater onto and across Antarctic ice shelves. *Nature* **544**, 349–352 (2017); corrigendum **551**, 658 (2017).
24. Bell, R. E. et al. Antarctic ice shelf potentially stabilized by export of meltwater in surface river. *Nature* **544**, 344–348 (2017).
25. Stokes, C. R., Sanderson, J. E., Miles, B. W. J., Jamieson, S. S. R. & Leeson, A. A. Widespread distribution of supraglacial lakes around the margin of the East Antarctic Ice Sheet. *Sci. Rep.* **9**, 13823 (2019); correction **10**, 1923 (2020).

26. Kingslake, J. et al. *Report on Antarctic Surface Hydrology Workshop, LDEO, 2018* (USAP DC, 2018); https://doi.org/10.15784/601170
27. Kuipers Munneke, P. K., Ligtenberg, S. R. M., Van Den Broeke, M. R. & Vaughan, D. G. Firn air depletion as a precursor of Antarctic ice-shelf collapse. *J. Glaciol.* **60**, 205–214 (2014).
28. Haran, T., Bohlander, J., Scambos, T., Painter, T. & Fahnestock, M. *MODIS Mosaic of Antarctica 2008–2009 (MOA2009) Image Map* (NSIDC, 2014).
29. Ronneberger, O., Fischer, P. & Brox, T. U-Net: convolutional networks for biomedical image segmentation. In *Medical Image Computing and Computer-Assisted Intervention–MICCAI 2015* (eds Navab, N. et al.) 234–241 (Springer International Publishing, 2015).
30. McGrath, D. et al. Basal crevasses on the Larsen C Ice Shelf, Antarctica: implications for meltwater ponding and hydrofracture. *Geophys. Res. Lett.* **39**, L16504 (2012).
31. McGrath, D. et al. Basal crevasses and associated surface crevassing on the Larsen C Ice Shelf, Antarctica, and their role in ice-shelf instability. *Ann. Glaciol.* **53**, 10–18 (2012).
32. Luckman, A. et al. Basal crevasses in Larsen C Ice Shelf and implications for their global abundance. *Cryosphere* **6**, 113–123 (2012).
33. Nye, J. F. The distribution of stress and velocity in glaciers and ice-sheets. *Proc. R. Soc. Lond. A* **239**, 113–133 (1957).
34. van der Veen, C. J. Fracture mechanics approach to penetration of bottom crevasses on glaciers. *Cold Reg. Sci. Technol.* **27**, 213–223 (1998).
35. Duddu, R., Jiménez, S. & Bassis, J. A non-local continuum poro-damage mechanics model for hydrofracturing of surface crevasses in grounded glaciers. *J. Glaciol.* **66**, 415–429 (2020).
36. Litwin, K. L., Zygielbaum, B. R., Polito, P. J., Sklar, L. S. & Collins, G. C. Influence of temperature, composition, and grain size on the tensile failure of water ice: implications for erosion on Titan. *J. Geophys. Res. Planets* **117**, E08013 (2012).
37. Fretwell, P. et al. Bedmap2: improved ice bed, surface and thickness datasets for Antarctica. *Cryosphere* **7**, 375–393 (2013).
38. van Wessem, J. M. et al. Modelling the climate and surface mass balance of polar ice sheets using RACMO2–Part 2: Antarctica (1979–2016). *Cryosphere* **12**, 1479–1498 (2018).
39. Poinar, K. et al. Drainage of Southeast Greenland firn aquifer water through crevasses to the bed. *Front. Earth Sci.* **5**, 5 (2017).
40. Lenaerts, J. T. M. et al. Meltwater produced by wind–albedo interaction stored in an East Antarctic ice shelf. *Nat. Clim. Change* **7**, 58–62 (2017).
41. Bell, R. E., Banwell, A. F., Trusel, L. D. & Kingslake, J. Antarctic surface hydrology and impacts on ice-sheet mass balance. *Nat. Clim. Change* **8**, 1044–1052 (2018).

Methods

Machine learning development and evaluation

To develop a machine learning model to detect ice-shelf fractures, we first trained several models on a training set to learn the relationships between input images and corresponding fractures labelled manually by visual inspection. Next, we assessed the performance of the trained models on a validation dataset with a range of hyperparameters. The best-performing model on the validation data was selected for evaluation on an unseen test dataset.

Training, validation and testing datasets. A 1,000 km × 1,000 km (8,000 pixels × 8000 pixels, at 125 m resolution) region covering the Larsen C and George VI ice shelves in the MODIS MOA[28,42] was used as the training and validation sets (Extended Data Fig. 1a). This subset of MOA contains fracture features near shear margins, calving fronts and grounding lines, covering the range of typical fracture patterns observed on Antarctic ice shelves. We first cropped the 8,000 pixel × 8,000 pixel image into smaller tiles (1,000 pixels × 1,000 pixels), of which 32 tiles contained ice-shelves (non-black areas in Extended Data Fig. 1a). We randomly divided the 32 tiles into a training set (26 image tiles) and a validation set (6 image tiles). To evaluate the developed machine learning model on an unseen dataset, we prepared an independent testing set consisting of 6 image tiles of size 1,000 pixels × 1,000 pixels randomly selected from the remaining continent-wide MODIS image.

Using a Matlab script, we manually labelled the datasets (38 tiles in total) by visually identifying fractures on the basis of their linear morphology and alignment perpendicular to flow (fractured areas are filled in white as shown in Extended Data Fig. 1c). The marked fractures were rasterized as binary labels. A sample training tile and its labels are shown in Extended Data Fig. 1b and c, respectively.

Model selection. For model selection, we compared the predictive performance of a wide range of machine learning models. We explored four sets of models, including (1) several single-layer convolutional neural networks (CNNs) with different filter sizes, 1 × 1, 28 × 28 and 56 × 56, (2) U-Net[29] using different numbers of first-layer feature maps (1, 2, 4, 16, 32, 64), (3) feature pyramid networks (FPNs)[43] with a ResNet-18 backbone, and (4) an edge detector[44] (using OpenCV's cv.Canny implementation with minimal threshold = 0 and maximum threshold = 255). There are many other advanced segmentation models such as DeepLabv3[45], SegNet[46], PSPNet[47], and others. Doing a detailed comparison for a wide range of advanced segmentation models to detect fractures on satellite imagery is left for future work.

We used the area under the receiver operating characteristics curve (AUC) as the evaluation metric for model selection. The AUC of the trained models on the validation set is plotted in Extended Data Fig. 2a(i) as a function of the total number of parameters in each model. All models were trained with a batch size of 1. The single-layer CNN and FPN models were trained using the stochastic gradient descent optimizer to minimize the cross-entropy loss. The U-Net was trained with the momentum optimizer to minimize the cross-entropy loss.

As shown in Extended Data Fig. 2a, the performance of U-Net increases greatly when the initial number of feature maps (d) increases from 1 to 4, reaching a maximum of AUC = 0.99 when d = 32, then slightly decreases when d increases beyond 32. Single-layer CNNs with filter sizes of 1 × 1, 28 × 28, and 56 × 56 perform well but do not exceed the performance of the U-Net when the number of parameters is increased. This is probably due to an insufficient number of layers to recognize complex fracture patterns. Lastly, the FPN is a state-of-the-art method for recognizing objects on the COCO dataset[48], however, it has an AUC of 0.82 for the fracture detection task in this study, which is lower than that of the U-Net. This is probably a result of overparameterization for this comparatively simple task. On the basis of these observations, we selected the U-Net with 32 initial feature maps for making predictions on the continent-wide map. A sample validation label and image are displayed in Extended Data Fig. 2c, d, respectively.

U-Net architecture. To detect fractures we employed the U-Net[29], a DCNN that has been successfully applied to image segmentation. In addition to a contracting path, which is typical for convolutional neural networks, the U-Net also contains an expansive path, which gives rise to its U-shaped architecture (Extended Data Fig. 1d). The expansive path recovers the location of the classified pattern and enables efficient use of training examples.

In our U-Net setup, there are 2 classes (fracture and non-fracture) in the output predictions, one channel in the input image (1,000 pixels × 1,000 pixels), 32 feature maps in the first layer and 13 convolutional layers (ten 3 × 3 convolutional layers, two 2 × 2 transposed convolutional layers, and one final 1 × 1 convolutional layer) in the entire architecture (Extended Data Fig. 1d). For each block in the contracting path, the image is convolved twice with 3 × 3 filters, each followed by a ReLU activation function, and down-sampled with a 2 × 2 max pooling (stride 2) filter. For each block in the expansive path, the image size is increased by a 2 × 2 upsampling (transposed convolutional) filter, followed by a concatenation with the cropped feature maps from the corresponding contracting layer, two 3 × 3 convolution filters and a ReLU activation function. The number of filters is halved and doubled in the downsampling and upsampling steps, respectively. Finally, a 1 × 1 convolution is applied to generate the output prediction (960 pixels × 960 pixels). We trained our model using the momentum optimizer with the hyperparameters (learning rate = 1.4, momentum = 0.2, decay rate = 0.95) that optimize the AUC on the validation set. A sample prediction of the fracture is shown in the right panel of Extended Data Fig. 1d.

Threshold selection. Next, a classification threshold was applied to the predictions (continuous output between 0 and 1, Extended Data Fig. 2e) so that every pixel was classified as either a fracture (white in Extended Data Fig. 2f) or non-fracture (black in Extended Data Fig. 2f). Every threshold corresponds to a point on the receiver operating characteristics (ROC) curve. Lower thresholds yield higher sensitivity (percentage of pixels with fractures that are classified as fractures) but lower specificity (percentage of pixels without fractures that are classified as non-fractures). We applied a range of thresholds (0–1) on the validation-set predictions and measure the F1 scores. The threshold (0.2) with the highest F1 score on the validation set was selected for generating the continent-wide fracture map shown in Fig. 2.

Evaluation using the testing set. Finally, we evaluated the model performance using the testing set not seen by the model. The model showed an AUC of 0.97 (95% CI: 0.93–0.99) on the testing set, as shown in Extended Data Fig. 2b. The CI of the model performance was calculated using bootstrapping with 1,000 samples. We further performed a data titration experiment to understand the impact of the training set size with respect to the performance. Increasing the number of training tiles from 6 to 26 only increases the AUC from 0.95 to 0.97, indicating that increasing the training dataset size further will probably not substantially improve performance. The classification performance on the testing set, after applying the classification threshold (0.2) to the predictions, showed a specificity of 0.99 and sensitivity of 0.64.

Continent-wide fracture map. We applied the final U-Net with the selected threshold to the continent-wide MOA imagery to identify fracture features across all ice shelves (marked in white in Fig. 2). Note that the resolution of the fracture map is 125 m, but the resolution of the strain rate data (Extended Data Fig. 6a) is 1 km (ref. [13]). We downsampled the fracture map to 1 km resolution to construct Fig. 3c using the fracture locations and strain rate data on the same grid. The downsampling algorithm used nearest-neighbour interpolation.

The images before and after downsampling are shown in Extended Data Fig. 2f, g, respectively. Some detailed fracture patterns are lost in the 1-km-resolution fracture map (Extended Data Fig. 2g) but the overall fracture distribution is retained. For future work, the proposed method can be extended to a finer grid where higher-resolution imagery (for example, Landsat) and strain rates are available[49].

Limitations on fracture identification. Most (89%) of the fractures mapped using 125-m-resolution MOA imagery lie in the region of the stability diagram (dimensionless tensile resistive stress and dimensionless fracture toughness) where our theory predicts that the tensile resistive stress exceeds the critical value required for dry surface fracturing. The remaining fracture locations fall in the region of parameter space where the theory predicts that no dry surface fractures should form. There are several possible explanations; for example, unresolved locally high strain rates, existing fractures advecting into lower-stress regions, incorrectly identified fractures, or fracturing resulting from more complex fracture modes than our theory describes.

The theory also predicts that dry surface fractures exist in many locations where the DCNN does not detect them. Several explanations for this are possible. First, the satellite imagery we used relies on a part of the electromagnetic spectrum where energy does not penetrate through snow and ice. It therefore fails to detect surface fractures buried by snow unless there is sufficient surface expression. For example, the presence of buried surface fractures can sometimes be inferred from the presence of elongated depressions in the snow surface, which may be observable in MOA. However, it is possible that many subsurface fractures were not detected by the DCNN because they had little or no surface expression. Satellite-based radar (for example, RADARSAT, SENTINEL-1) can detect sub-surface structures because radio waves penetrate up to ~10 m into the subsurface[50,51]. Applying the DCNN to these data may allow us to test whether buried surface fractures are widespread in these regions, as predicted by the theory. Second, it is possible that the limitations of the DCNN are causing us to fail to detect surface fractures in these locations. Although the performance of the DCNN output prediction (a continuous variable ranging from 0 to 1) evaluated against testing set is excellent (AUC = 0.97), the binary classification of fracture features (a binary variable, either 0 or 1) identified via application of a classification threshold yielded a sensitivity of 0.64, indicating that 37% of all fracture features manually labelled on the test data were not detected by the DCNN. The performance of the U-Net is expected to improve if higher resolution imagery are used. It is also possible that the relatively low-resolution imagery is incapable of detecting crevasses smaller than a few hundred metres in length or width, and we therefore failed to detect many smaller crevasses in the locations where the theory predicts that they should form. Future work could apply the DCNN within a high-performance computer framework to higher-resolution imagery.

Theory of ice-shelf fractures

We have developed a model of ice-shelf fracturing based on linear elastic fracture mechanics (LEFM). A complete theoretical description is available in the Supplementary Information, which draws on refs. [1,2,18,33–36,52–57]. The Supplementary Information describes LEFM for surface crevasses (Supplementary Section 1) and basal crevasses (Supplementary Section 6), the determination of dimensionless parameters (equation (1)) for the fracture stability diagram (Fig. 3c), the derivation of the critical stress required for surface crevasse formation (equation (2); Supplementary Section 3), firn effects on surface crevasses (Supplementary Section 2), surface crevasse depth from LEFM versus Nye's zero-stress approximation (Supplementary Section 4), water-filled crevasse stability and initial flaws (Supplementary Section 5) and the effects of vertical englacial temperature gradients on surface and basal fractures (Supplementary Section 7). Using theoretical results derived in the Supplementary Information, we discuss the stability of surface and basal fractures below.

Physical regimes of surface and basal fractures. The stability diagram for surface and basal fractures is shown in Extended Data Fig. 4d. We labelled physical regimes I–V on the stability diagram, marked the ice-shelf locations corresponding to each regime (Extended Data Fig. 4e–h) and quantitatively shown the percentage of ice shelves corresponding to each physical regime. The four panels (Extended Data Fig. 4e–h) show the variability in the location of each regime when different ice-shelf stress datasets were used (their corresponding stability diagrams are shown in Fig. 3c and Extended Data Fig. 8). Locations where basal fractures are stable (blue; regime III) cover 41–62% of ice shelves and are theoretically dominant on ice shelves. Locations where surface fractures could theoretically form are widespread and overlap with that of stable and unstable basal fractures. The locations of unstable basal fractures (red; regime IV) cover only 2–4% of the total ice-shelf area. These red areas largely overlap with areas of high extensional stress downstream of pinning points where ice is damaged or near existing rifts, as shown in Extended Data Fig. 4e–h, with close-up examples shown in the second row. Note that the red area is purely an output from a given dimensionless stress input, and is independent of the neural network-mapped fracture-feature locations (white locations).

Within this 2–4% area (regime IV; red in Extended Data Fig. 4e–h) the effective viscosity could be overestimated in locations with highly damaged ice. Some red areas that coincide with fracture features disappear when the stress field from Fürst et al.[13] is used directly (Extended Data Fig. 4g, h), as this product inherently includes the damage-induced softening of the ice. On the other hand, LEFM may be unable to accurately describe basal fracture stability. For example, ice may be more ductile[58] at the base and thus require more energy to break than predicted by LEFM, thus stabilizing basal crevasses that would be unstable according to LEFM and reducing the red areas in Extended Data Fig. 4e–h.

Data used for the fracture stability diagram

Data sources. The parameters required to plot ice-shelf locations on the stability diagram of dimensionless tensile resistive stress and dimensionless fracture toughness are tensile resistive stress R_{xx}, ice thickness H, fracture toughness K_{Ic} and ice density ρ_{i}. The stress was calculated using the strain rate $\dot{\epsilon}_{xx}$ and the effective viscosity, which was calculated using the viscosity factor B, according to Glen's flow law $R_{xx} = 2B\dot{\epsilon}_{xx}^{1/n}$. We used the along-flow strain rate $\dot{\epsilon}_{xx}$ (Extended Data Fig. 6a) determined from a model assimilation of satellite-derived velocity data[13,59]. The assimilated velocity field effectively smoothed the observed velocity field[60], which can otherwise be problematic when differentiating to compute strain-rate fields[61]. An alternative approach is to use the first principal strain rate. In the next section we demonstrate that using the first principal stress instead of the along-flow stress does not impact our main conclusions. Ice-shelf thickness was from Bedmap2[37] (Extended Data Fig. 6b). The viscosity factor B (Extended Data Fig. 6c) was calculated using an empirical function, which is dependent on ice temperature (equation (6) in ref. [57]). Most surface fractures are 1–50 m deep (less than 25% of the typical ice thickness), and the ice temperature within this range is approximately constant (fig. 1b in ref. [62]). Thus, we calculated B using the surface temperature T_{s} (Extended Data Fig. 6d), obtained from a time average of the regional climate model RACMO2.3p2. The negligible effect of vertical temperature gradient on the surface fracture stability is addressed in Supplementary Section 7 and Extended Data Fig. 9. The fracture toughness is insensitive to temperature in the range 100–273.15 K according to laboratory measurements (figure 3 in ref. [36]), and thus was assumed constant $K_{\mathrm{Ic}} = 150$ kPa m$^{1/2}$ (ref. [36]) across ice shelves in our study. Note that an alternative approach is to use the stresses computed directly by the model assimilation ref. [13]. This has the advantage that the effects of ice damage (for example, due to crevassing) are accounted for in the

ice viscosity, but this does not impact our main conclusions (Extended Data Fig. 8).

Stability diagram for all ice shelves and 2D histogram. The axes of the fracture stability diagram (Fig. 3c) are dimensionless fracture toughness $\tilde{K}_{Ic}$ and tensile resistive stress $\tilde{R}_{xx}$ (equation (1)), which control whether fractures occur (equation (2)) and their stability. $\tilde{K}_{Ic}$ and $\tilde{R}_{xx}$ were calculated on a 1 km × 1 km grid using the datasets identified in the previous section. These values are plotted as red dots in Extended Data Fig. 7 (n = 1,258,908 points), showing the range of parameter values across all ice shelves. The subset of locations where fractures were identified by the deep convolutional neural network (DCNN) are marked in yellow (n = 31,962) in Extended Data Fig. 7. These points almost exclusively lie within the stable-fracture phase.

To visualize the density of points in Extended Data Fig. 7, we plot the two-dimensional histogram for the fracture locations (yellow dots) in Fig. 3c in the main text. The data points were sorted into bins with logarithmically varying widths for both axes (that is, data in the range of $10^{x} - 10^{x+0.01}$ was sorted into the same bin). The total number of data points within each bin is denoted by the colour (Fig. 3c). This shows a dense population of fracture features within the parameter regime where we predict stable surface and basal fractures and demonstrates a remarkable agreement with our analytical result (red line, equation (2)) for the transition boundary between the no-surface-fracture and stable-surface-fracture regions of the stability diagram.

Uncertainties associated with our choices of stress and strain-rate fields. The tensile resistive stresses R_{xx} used in the stability diagram and vulnerability map in Fig. 3c and Fig. 4 were calculated from the surface-temperature-dependent viscosity factor $B(T)$ and the along-flow strain rate $\dot{\epsilon}_{xx}$ computed by Fürst et al.[13]. In Fig. 4 the areas that both generate substantial buttressing and are vulnerable to hydrofracture are marked in red and cover 60% of total ice-shelf area. To check the sensitivity of our results to the strain rates, we repeated our analysis using along-flow strain rates supplied by ref. [61] (Extended Data Fig. 8a). These strain rates were derived by applying Gaussian smoothing to the MEaSUREs V2 Antarctic velocity product[60,63]. We found fewer points within the no-surface-fracture regime and an increase in the extent of the vulnerable regions (69% in Extended Data Fig. 8a compared with 60% in Fig. 4a).

The impact of ice damage on ice viscosity[64] is not considered in the main text but included in Extended Data Fig. 8b, c. More damaged ice is less viscous and therefore experiences less stress for a given strain rate. The stresses calculated by ref. [13] incorporated an inverted viscosity parameter, which was calculated so that model velocities matched observations[60]. The effects of damage were therefore embedded in the computed stresses. Extended Data Fig. 8b, c show the stability diagram and vulnerability maps computed using the along-flow stress and first principal stress (that is, maximal tensile resistive or minimal compressive stress) determined by ref. [13]. The difference between the distributions of data within the stability diagrams is small.

The conclusions drawn from our analysis of the stability diagram and vulnerability map are unaffected by these choices regarding strain rates and stresses. First, most fracture features fall in the predicted physical regime (below the red theoretical curve). Second, large portions of the area vulnerable to hydrofracture (red regions in the lower panel in Extended Data Fig. 8) provide substantial buttressing (outside the passive ice-shelf areas; blue).

Advection of fractures and stress history. Although we evaluated the physical conditions (dimensionless stress and toughness; equation (1)) at the present-day locations of the observed fractures, brittle fractures likely had initially formed upstream of these locations and had been advected downstream. During this time they probably deformed viscously, causing the fracture to widen such that it can be seen in the 125-m-resolution satellite image. We tracked the stress upstream along streamlines (assuming steady flow) for all fracture features and identified the maximum dimensionless stress $\tilde{R}_{xx\max}$ that the fracture had experienced since crossing the grounding line. For each fracture location detected by the DCNN, we then plotted $\tilde{R}_{xx\max}$ and the corresponding dimensionless toughness at the location where maximum dimensionless stress occurs, as shown in Extended Data Fig. 9b. Compared with $\tilde{R}_{xx}$ and $\tilde{K}_{Ic}$ evaluated at the locations of the fracture features, Extended Data Fig. 9a, the points evaluated at the locations of the maximum dimensionless stresses are shifted to the right, so are still in the physical regime where the theory predicts stable surface fractures. This shows that although brittle fractures can form upstream at higher stresses compared to their current locations, most of them (89%) remain in the physical regime where LEFM predicts stable surface fractures, after they are advected downstream to their current locations. Note that, from the MOA images we do not know exactly where or when each fracture initially forms, but we do know that the majority of the surface fractures experience physical conditions that allow brittle surface fracture both at their maximum stress in the past (Extended Data Fig. 9b) and their current stress state (Extended Data Fig. 9a). We thus used equation (2) (the analytical solution for the boundary between the no-surface-fracture/stable-surface-fracture regimes based on LEFM; red line in Extended Data Fig. 9) to estimate the areas where physical conditions allow the formation of dry, stable and brittle surface fractures before they can later deform viscously and advect downstream. These areas are vulnerable to hydrofracture (red area in Fig. 4a) because water-filled fractures are unstable (from both LEFM and zero-stress approximation).

The surface expression of basal crevasses. As described in the main text, a subset of the fracture features identified by the DCNN could be surface expressions of basal crevasses[30–32]. Although the DCNN was not trained to distinguish surface expressions of basal crevasses[30–32] from surface fractures, we note that the two features are not mutually exclusive and very often coexist[31] (to comprehensively distinguish these two features continent-wide radar profiles showing basal crevasse would be required). As noted by Bassis and Ma[58], a sufficiently wide basal crevasse can induce tensile stress near the surface large enough to create surface fractures. Most importantly, we showed that most DCNN-identified fracture features (related to basal crevasses or not) occur where dimensionless stresses are sufficient to form stable dry surface fracture (Fig. 3c).

Lake locations

Stokes' supraglacial lake locations compared with vulnerability map. Stokes et al.[25] mapped supraglacial lakes in Landsat imagery from January 2017 across all East Antarctic ice shelves (defined using BedMap2's[37] ice-shelf mask). Plotting their lake locations on our map of vulnerability to hydrofracture (Extended Data Fig. 10), we see that most lakes lie in the resilient regions (yellow–green areas).

To obtain an upper estimate of the proportion of East Antarctic ice shelves that experience meltwater ponding and are vulnerable to hydrofracture, we summed the areas of the 1 km × 1 km grid boxes that contain lakes and lie in the vulnerable regions, then divided by the total area of East Antarctic ice shelves, to give ~0.63%. The proportion of East Antarctic ice shelves that lie at the intersection of all three circles in Fig. 1 (that is, have meltwater ponds, are vulnerable to hydrofracture and provide substantial buttressing) is approximately the same (~0.6%) because Stokes' lakes mostly lie in places providing substantial buttressing (as identified by Fürst et al.[13]). Note that areas of most individual lakes are ~0.001–0.01 km^2 (see figure 3a in ref. [25]) — much smaller than the spatial resolution (1 km^2) of our vulnerability map. Thus the true overlaps between these regions may be two to three orders of magnitude smaller than estimated here.

Data availability

The training, validation, and testing datasets are available at https://github.com/chingyaolai/Antarctic-fracture-detection and https://doi.org/10.5281/zenodo.3949427. The neural-network mapped fracture locations on the MOA 2009 (125 m resolution) imagery (Fig. 2) and the data required to construct the vulnerability map (Fig. 4) are available at https://doi.org/10.15784/601335. MOA (2009) imagery (https://doi.org/10.7265/N5KP8037) is available at the National Snow and Ice Data Center (NSIDC). Strain-rate fields are calculated from the dataset SUMER Antarctic Ice-shelf Buttressing, Version 1 (https://doi.org/10.5067/FWHORAYVZCE7) available via the NSIDC. Ice-shelf thickness data are from Bedmap2 (https://www.bas.ac.uk/project/bedmap-2/). The surface temperature data from the RACMO2.3p2 regional climate model are available from J.M.v.W. (j.m.vanwessem@uu.nl).

Code availability

The code for our experiment is available at https://github.com/chingyaolai/Antarctic-fracture-detection (https://doi.org/10.5281/zenodo.3949427). The U-Net implementation[65] is available at https://github.com/jakeret/tf_unet. The FPN implementation is available at https://github.com/qubvel/segmentation_models. The deep learning framework, TensorFlow, is available at https://www.tensorflow.org/. Scripts for calculating the fracture stability diagram (Fig. 3c) are available from the corresponding author upon request.

42. Scambos, T. A., Haran, T. M., Fahnestock, M. A., Painter, T. H. & Bohlander, J. MODIS-based Mosaic of Antarctica (MOA) data sets: continent-wide surface morphology and snow grain size. *Remote Sens. Environ*. **111**, 242–257 (2007).
43. Lin, T.-Y. et al. Feature pyramid networks for object detection. In *2017 IEEE Conf. Computer Vision and Pattern Recognition* 936–944 (IEEE, 2017).
44. Canny, J. A computational approach to edge detection. *IEEE Trans. Pattern Anal. Mach. Intell.* **8**, 679–698 (1986).
45. Chen, L.-C., Zhu, Y., Papandreou, G., Schroff, F. & Adam, H. Encoder-decoder with atrous separable convolution for semantic image segmentation. In *Computer Vision–ECCV 2018* (eds Ferrari, V. et al.) 833–851 (Springer, 2018).
46. Badrinarayanan, V., Kendall, A. & Cipolla, R. SegNet: a deep convolutional encoder-decoder architecture for image segmentation. *IEEE Trans. Pattern Anal. Mach. Intell.* **39**, 2481–2495 (2017).
47. Zhao, H., Shi, J., Qi, X., Wang, X. & Jia, J. Pyramid scene parsing network. In *2017 IEEE Conf. Computer Vision and Pattern Recognition* 6230–6239 (IEEE, 2017).
48. Lin, T.-Y. et al. Microsoft COCO: common objects in context. In *Computer Vision–ECCV 2014* (eds Fleet, D. et al.) 740–755 (Springer International Publishing, 2014).
49. Fahnestock, M. et al. Rapid large-area mapping of ice flow using Landsat 8. *Remote Sens. Environ*. **185**, 84–94 (2016).
50. Rignot, E., Echelmeyer, K. & Krabill, W. Penetration depth of interferometric synthetic-aperture radar signals in snow and ice. *Geophys. Res. Lett*. **28**, 3501–3504 (2001).
51. Gray, L., Conway, H., King, E. & Smith, B. Flow stripes, GPR stratigraphy and RADARSAT imagery. *J. Glaciol*. **54**, 936–938 (2008).
52. Irwin, G. R. Analysis of stresses and strains near the end of a crack traversing a plate. *J. Appl. Mech*. **24**, 361–364 (1957).
53. Tada, H., Paris, P. C. & Irwin, G. R. *The Stress Analysis of Cracks Handbook* 3rd edn (Professional Engineering Publishing, 2000).
54. Gagliardini, O. & Meyssonnier, J. Flow simulation of a firn-covered cold glacier. *Ann. Glaciol*. **24**, 242–248 (1997).
55. van der Veen, C. J. *Fundamentals of Glacier Dynamics* (CRC, 2013).
56. Griffith, A. A. The phenomena of rupture and flow in solids. *Phil. Trans. R. Soc. A* **221**, 163–198 (1921).
57. Hooke, R. L. Flow law for polycrystalline ice in glaciers: comparison of theoretical predictions, laboratory data, and field measurements. *Rev. Geophys*. **19**, 664-672 (1981).
58. Bassis, J. N. & Ma, Y. Evolution of basal crevasses links ice shelf stability to ocean forcing. *Earth Planet. Sci. Lett*. **409**, 203–211 (2015).
59. Durand, G., F. Gillet-Chaulet, O. Gagliardini, J. J. Fürst. SUMER Antarctic Ice-shelf Buttressing, Version 1. (NSIDC, 2016); https://doi.org/10.5067/FWHORAYVZCE7
60. Rignot, E., Mouginot, J. & Scheuchl, B. Ice flow of the Antarctic Ice Sheet. *Science* **333**, 1427–1430 (2011).
61. Wearing, M. *The Flow Dynamics and Buttressing of Ice Shelves* PhD thesis. Univ. Cambridge (2017).
62. Rezvanbehbahani, S., Veen, C. J. & Stearns, L. A. An improved analytical solution for the temperature profile of ice sheets. *J. Geophys. Res. Earth Surf*. **124**, 271–286 (2019).
63. Rignot, E., Mouginot, J. & Scheuchl, B. *MEaSUREs InSAR-Based Antarctica Ice Velocity Map, Version 2* (NSIDC, 2017); https://doi.org/10.5067/D7GK8F5J8M8R
64. Borstad, C. et al. A constitutive framework for predicting weakening and reduced buttressing of ice shelves based on observations of the progressive deterioration of the remnant Larsen B Ice Shelf. *Geophys. Res. Lett*. **43**, 2027–2035 (2016).
65. Akeret, J., Chang, C., Lucchi, A. & Refregier, A. Radio frequency interference mitigation using deep convolutional neural networks. *Astron. Comput*. **18**, 35–39 (2017).

Acknowledgements We thank R. Bell, T. Scambos, R. Duddu, O. Sergienko and B. Minchew for discussions. We acknowledge the National Science Foundation for funding via grant no. OPP-1743310. C.-Y.L. thanks the Lamont-Doherty Earth Observatory for funding through the Lamont Postdoctoral Fellowship. J.M.v.W. acknowledges the Dutch Research Council (NWO) for funding through Veni grant no. VI.Veni.192.083. Disclaimer: For P.-H.C.C., the work was done in personal time. The views expressed in this article are those of the authors and do not necessarily reflect the official policy or position of Google LLC.

Author contributions C.-Y.L. led the project and the preparation of the manuscript. C.-Y.L. and J.K. designed the research. M.G.W. helped with development of the research, contributed strain rate data and ideas related to buttressing. C.-Y.L. developed the fracture model and the stability diagram. P.-H.C.C. provided guidance regarding the selection and evaluation of machine learning models. C.-Y.L. conducted the machine learning experiments and P.-H.C.C., P.G. and H.L. assisted with the neural networks. J.J.S. prepared the Landsat images. J.M.v.W. provided RACMO2.3p2 climate model output. C.-Y.L. wrote the manuscript with help from J.K., M.G.W., and P.-H.C.C. and input from all authors. All authors contributed to discussions of the research.

Competing interests P.-H.C.C. is an employee of Google and owns Alphabet stock. Other authors declare no competing interests.

Additional information
Supplementary information is available for this paper at https://doi.org/10.1038/s41586-020-2627-8.
Correspondence and requests for materials should be addressed to C.-Y.L.
Peer review information *Nature* thanks Jeremy Bassis, Javier Plaza, Stephen Price, Xiaoxiang Zhu and the other, anonymous, reviewer(s) for their contribution to the peer review of this work.

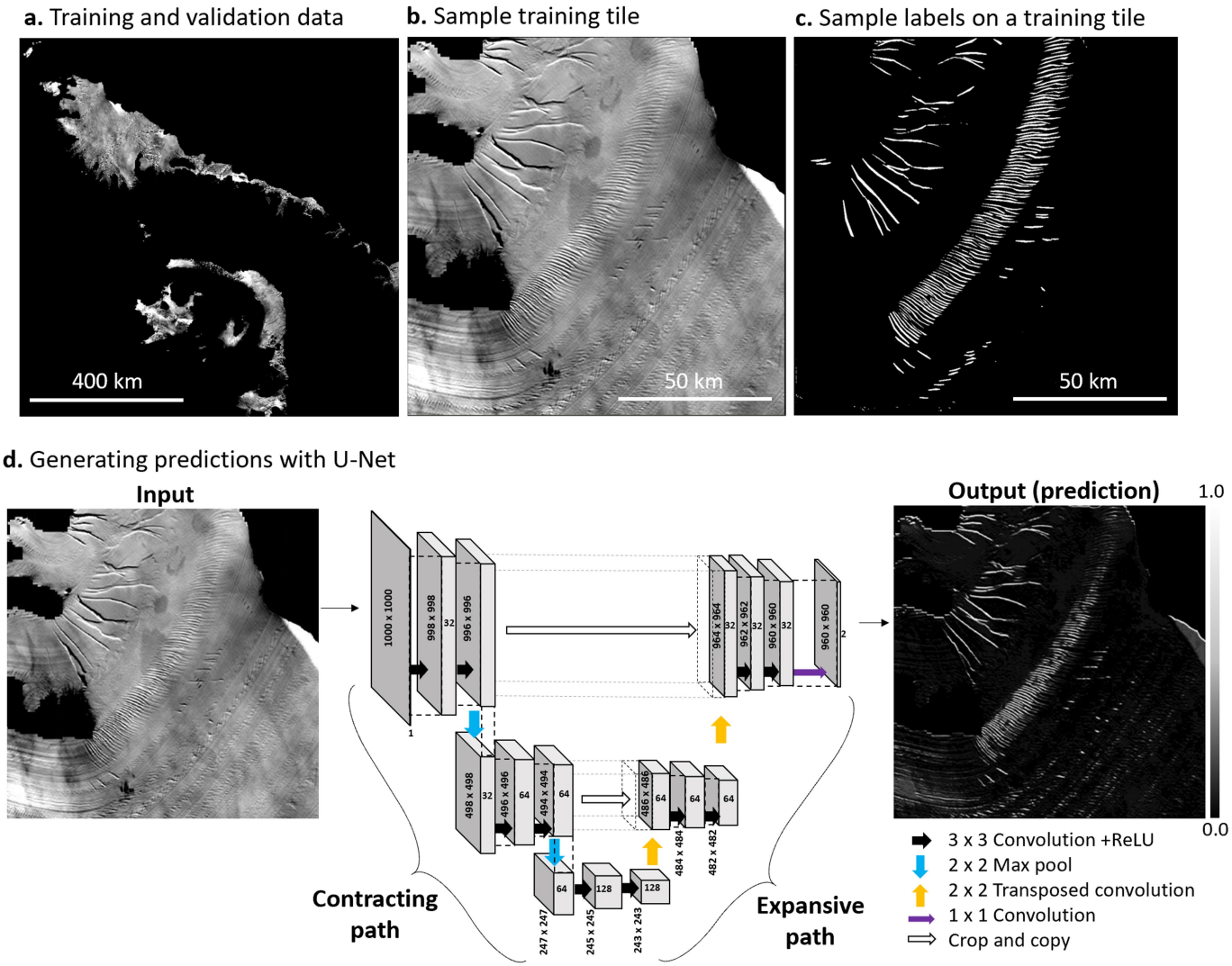

Extended Data Fig. 1 | Data preparation and the neural network architecture. a, The training and validation data were taken from a 8,000 pixel × 8,000 pixel subset (covering the Larsen and George VI ice shelves) of the 125-m-resolution MODIS imagery, which produced 32 tiles of 1,000 pixel × 1,000 pixel images containing ice shelves. The tiles were randomly separated into training (26 tiles) and validation (6 tiles) sets. **b**, Example of a training tile. **c**, The corresponding labels with white pixels indicating fractures. **d**, The U-Net architecture. The contracting and expansive paths give the U-Net[29] its U-shaped architecture. Arrows illustrate operations within the network and at each stage the data dimension is noted. The input image (left) is 1,000 pixels × 1,000 pixels with one channel and the output prediction (right) of the U-Net contains two classes (fracture and non-fracture).

a. (i) Model comparison

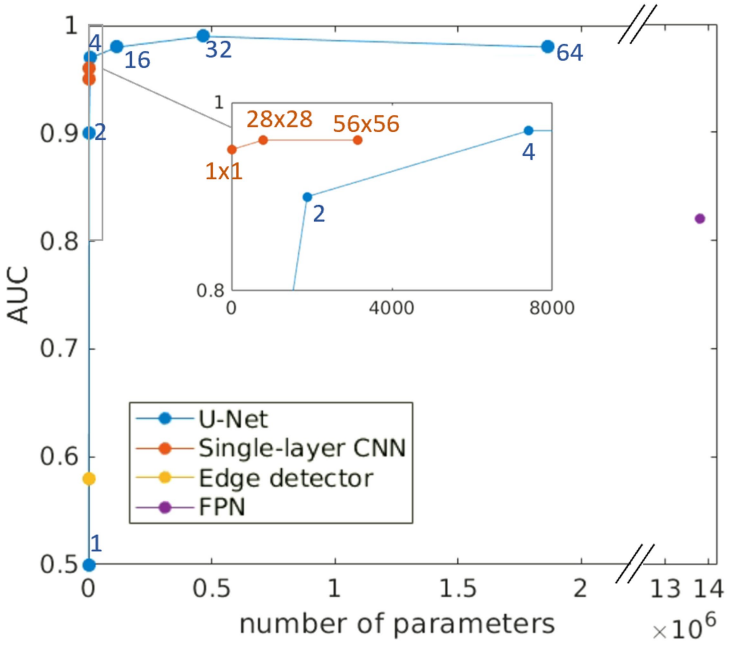

(ii) AUC comparison

U-Net			Single-layer CNN			Edge detector		FPN	
d	*N*	AUC	*k*	*N*	AUC	*N*	AUC	*N*	AUC
1	490	0.50	1	2	0.95	0	0.58	13,809,092	0.82
2	1,886	0.90							
4	7,402	0.97	28	785	0.96				
16	116,770	0.98							
32	465,986	0.99	56	3,137	0.96				
64	1,861,762	0.98							

b. Performance on testing data

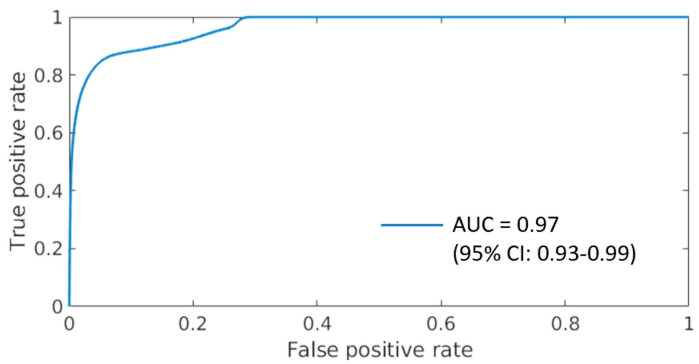

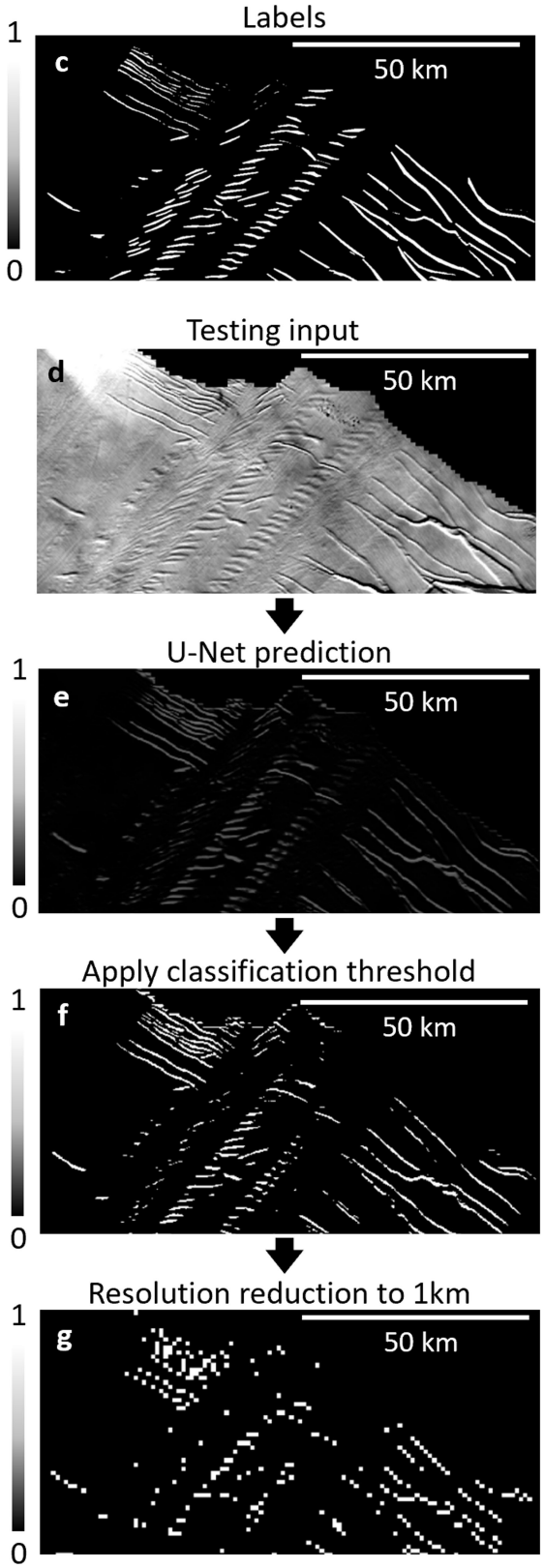

Extended Data Fig. 2 | Performance of the DCNN and fracture classification. **a**, (i), Comparisons of AUC for the validation data over number of parameters (*N*) for an edge detector[44], single-layer CNN with different filter sizes (1 × 1, 28 × 28, 56 × 56; denoted by *k*), U-Net with different depths of first-layer feature maps (1, 2, 4, 16, 32, 64; denoted by *d*) and FPN[43] using a ResNet-18 backbone. (ii), The AUCs and *N* values of each model evaluated against the validation data are summarized in the table. **b**, The performance of the U-Net (with *d* = 32) evaluated against an unseen testing set is shown by the ROC curves. **c**, **d**, Examples of validation label images (**c**) and original MOA images (**d**). **e**, Output of the model, continuous values between 0 and 1. **f**, Binarized classification of fractures that used a threshold (0.2), maximizing the F1 score on the validation set. Fracture features with predictions exceeding the threshold are marked in white. **g**, The resolution of the fracture map was reduced to 1 km, the resolution of the strain rate data, before we incorporated the DCNN result with other data in Extended Data Fig. 6.

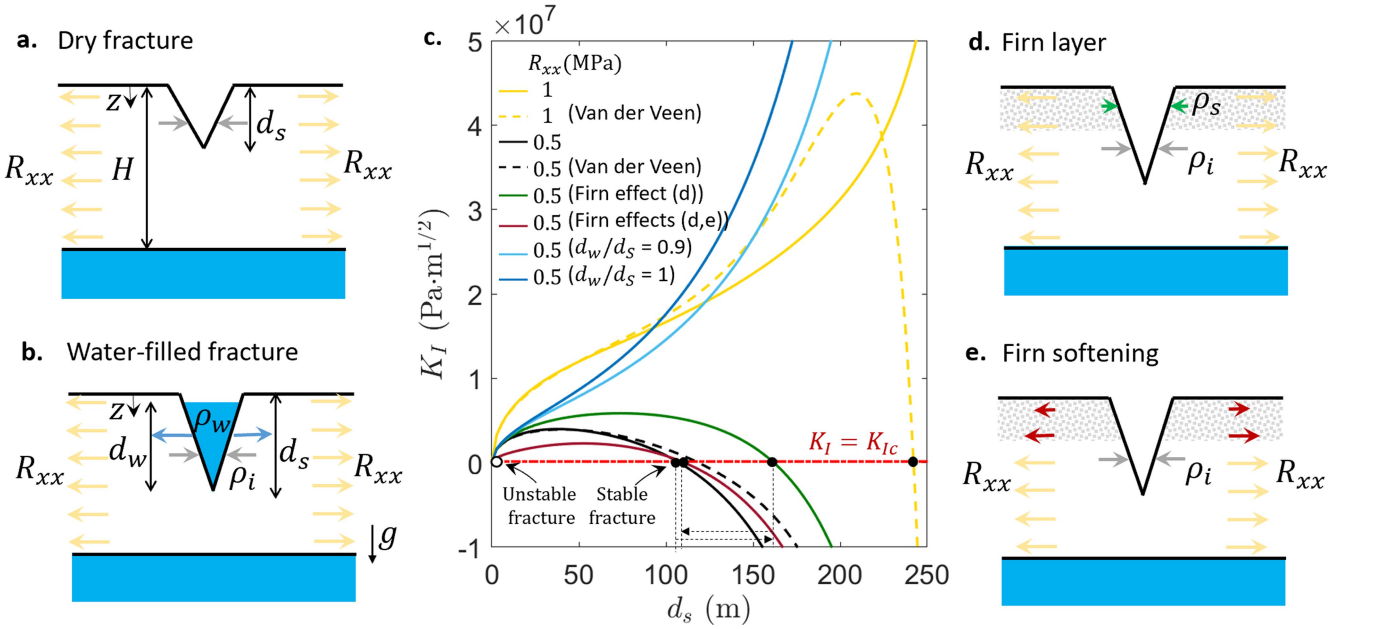

Extended Data Fig. 3 | Stresses acting on a surface fracture and fracture stability. a, **b**, The effects of tensile resistive stress, hydrostatic stress of water and overburden stress of ice on opening or closing of a surface fracture in dry (**a**) and water-filled fractures (**b**). **c**, The stress intensity factor (K_I) as a function of surface fracture depth (d_s) (Supplementary equation (5)) computed with R_{xx} = [0.5, 1] MPa, H = 300 m, surface firn density ρ_s = 400 kg m^{-3} and C = 0.02 m^{-1} (see Supplementary equation (6); ref. [2]). (The solution derived in this work is shown with a solid curves and that of Van der Veen (ref. [2]) by dashed curves.) **d**, **e**, The additional impacts of a firn layer are due to reduced density (**d**) and reduced viscosity (**e**). Reduced overburden stress due to lower density firn compared with ice acts to deepen surface fractures (black dot on green curve in **c**). In contrast, the reduced tensile resistive stress due to the reduced firn viscosity reduces surface fracture depth. The net effects of firn, shown by the red curve in **c**, are secondary compared with the effects from tensile resistive and overburden stresses of ice. We therefore did not include the effect of firn in the main analysis.

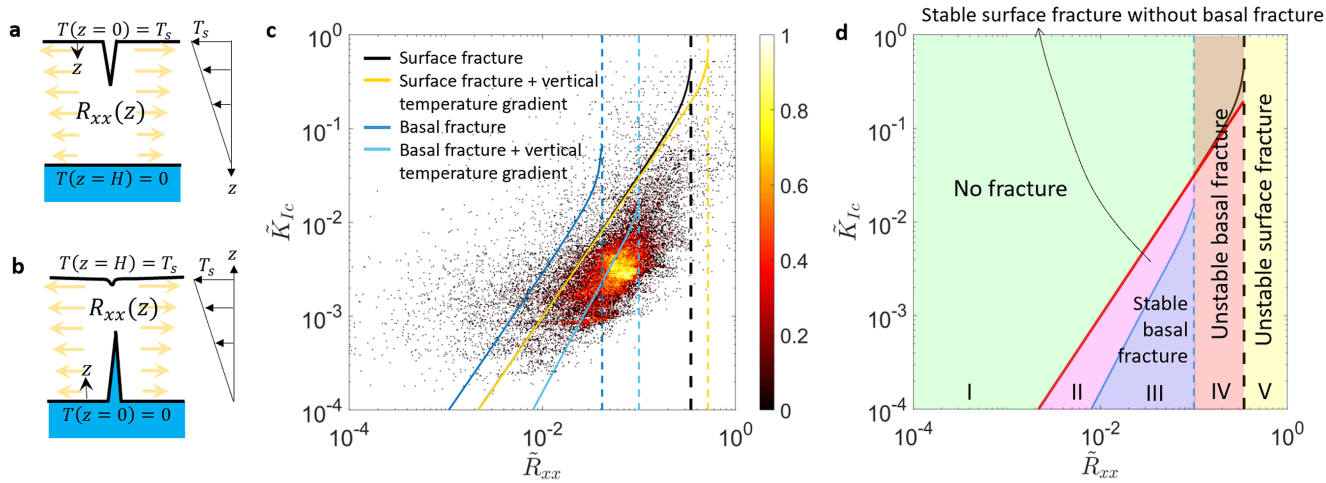

	e. Furst's strain rate + B(T)	f. Wearing's strain rate and B(T)	g. Furst's along-flow stress	h. Furst's 1st principal stress
I	27%	22%	34%	19%
II	21%	21%	26%	28%
III	53%	62%	41%	50%
IV	4%	3%	2%	3%
V	0.4%	0.5%	0.1%	0.2%

Extended Data Fig. 4 | Physical regimes of surface and basal fractures. **a**, **b**, The schematics of a surface (**a**) and basal crevasse (**b**) with depth varying resistive stress $R_{xx}(z)$ due to the vertical temperature gradient (assumed to be linear). **c**, The fracture stability diagram for surface and basal crevasses with and without temperature effects (assuming the surface and the base of ice shelf are −30 and 0 °C, respectively). Dashed and solid lines represent the transition boundaries of stable-to-unstable and no fracture-to-stable fracture regions, respectively. Warmer ice at the base reduces the ice viscosity (and thus stress), which impacts the locations of the stability boundaries of basal crevasse. **d**, The five physical regimes (I–V) defined by the transition boundaries for surface crevasse (black curves in **c**) and basal crevasse with temperature effects (light blue curves in **c**). **e**–**h**, The locations corresponding to regimes I–V on ice shelves are determined by different estimates of stress. The percentage values denote the portion of ice-shelf area containing the physical condition in each regime. The green, pink, blue, red, yellow and white areas correspond to regimes I, II, III, IV, V and the U-Net-detected fracture locations, respectively. **e**, **f**, The stress field determined by the temperature dependent viscosity factor $B(T)$ (equation (6) in ref. [57]) combined with along-flow strain rates obtained by Fürst et al.[13] (**e**) and Wearing[61] (**f**). **g**, **h**, The stress fields in the along-flow (**g**) and 1st principal (**h**) stress directions calculated by ref. [13] include the effects of damage-induced ice softening through the data assimilation and model inversion process. The second row of **e**–**h** is the close-up view of the white box in the first row. Note that the spatial areas of regimes I–V were calculated solely on the basis of the dimensionless stress and toughness, and are independent of the U-Net result. The spatial resolution is 1 km, the same as the stress field resolution used in ref. [13].

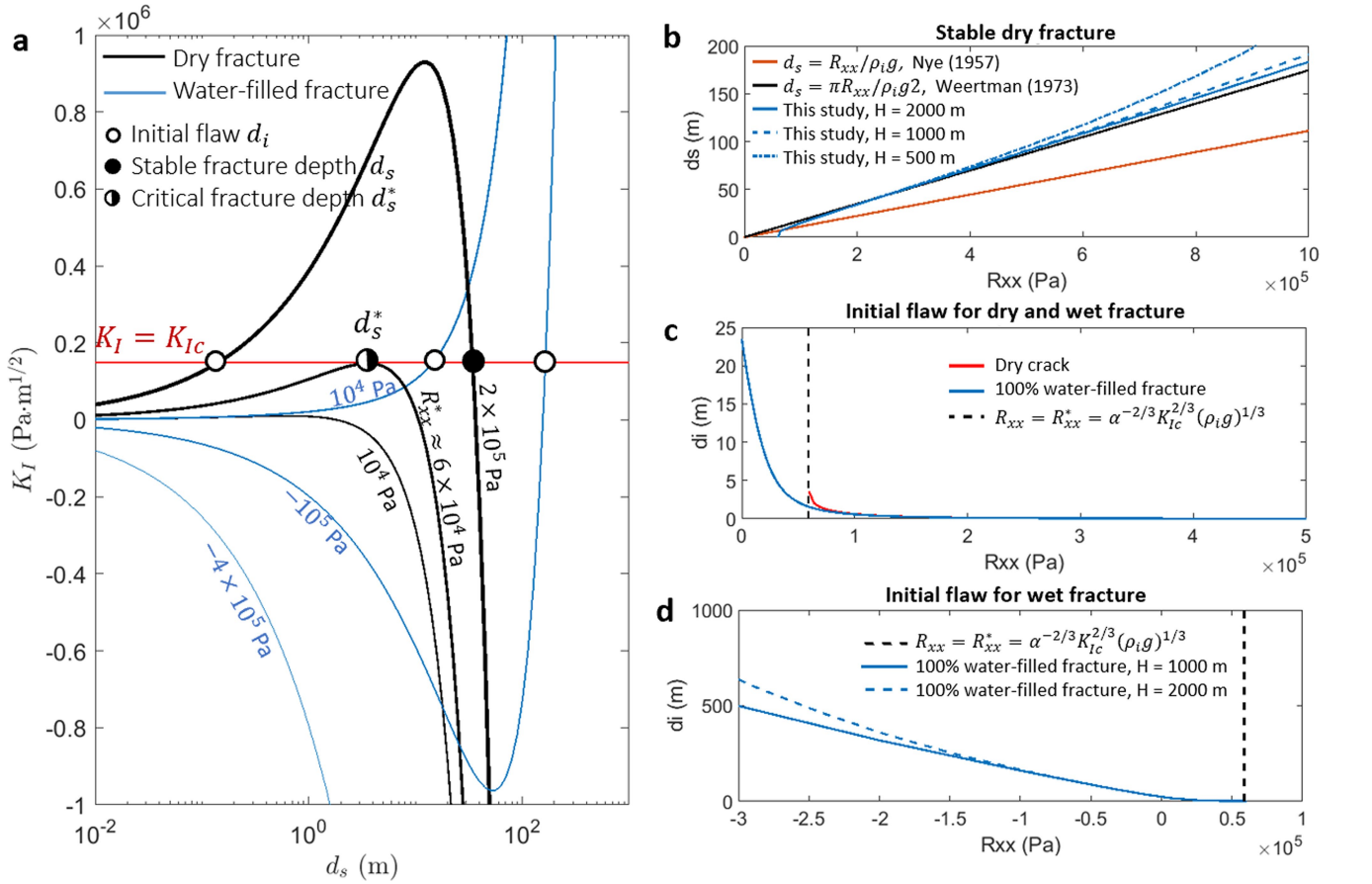

Extended Data Fig. 5 | Comparison between dry and water-filled fractures in LEFM. a, The stress intensity factor (Supplementary equation (5)) as a function of surface fracture depth was calculated for hydrofractures (blue curves) and dry surface fractures (black curves) for H=1,000 m. The number alongside each curve is the corresponding R_{xx}. Above the critical stress $R_{xx}^* \approx$ 60 kPa (calculated using equation (2) and $K_{Ic} \approx$150 kPa m$^{1/2}$) dry-surface-fracture depths are stable (black dot). Hydrofractures can become unstable when a pre-existing flaw filled with water reaches a depth denoted by the white dots. Water-filled initial flaws smaller than d_i will remain closed. When stress is sufficiently compressive, water-filled fractures will not grow (for example, the blue curve has negative slopes for any surface fracture depth below the red line). **b**, Comparison of d_s with previous theories. Our numerical solution approaches Weertman's solution at large ice thickness. **c**, **d**, The required d_i to destabilize a hydrofracture as a function of stress is shown by blue curves. The pre-existing flaw depths required to initialize stable dry surface fractures are plotted as a red curve in **c**, and reach a maximum of ~3.8 m at the critical stress R_{xx}^* (dashed line). Note that at R_{xx}^* the required initial flaw depth is the same as fracture depth, that is, $d_i = d_s = d_s^* \approx$ 3.8 m (half-white half-black dot in **a**).

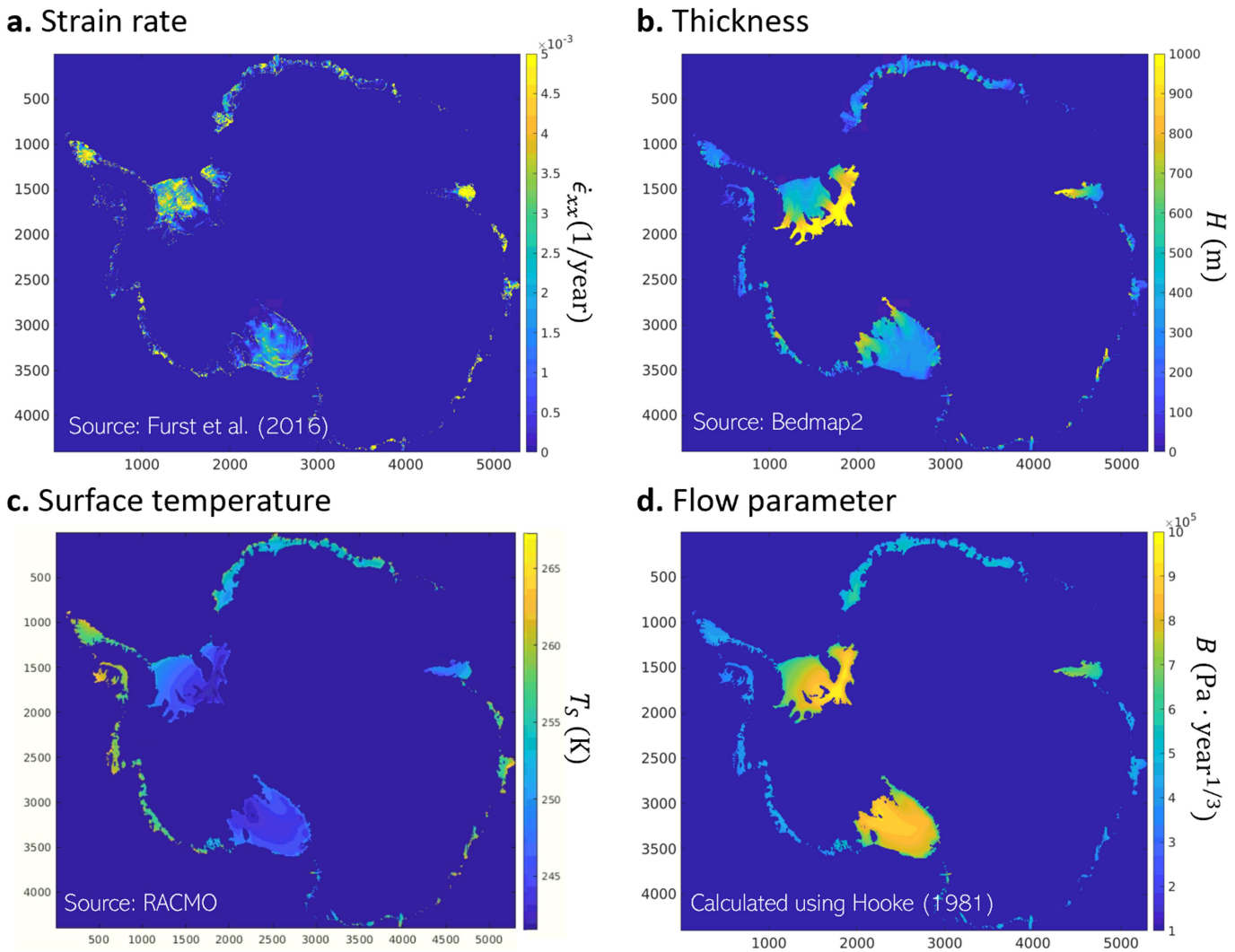

Extended Data Fig. 6 | Antarctic-wide data used to predict vulnerability to hydrofracture. a–**d**, The dimensionless toughness and dimensionless stress were evaluated using strain rates (**a**), ice-shelf thickness (**b**), surface temperature (**c**) and viscosity factor B (**d**, calculated from surface temperature) and plotted on the fracture stability diagram (Fig. 3c).

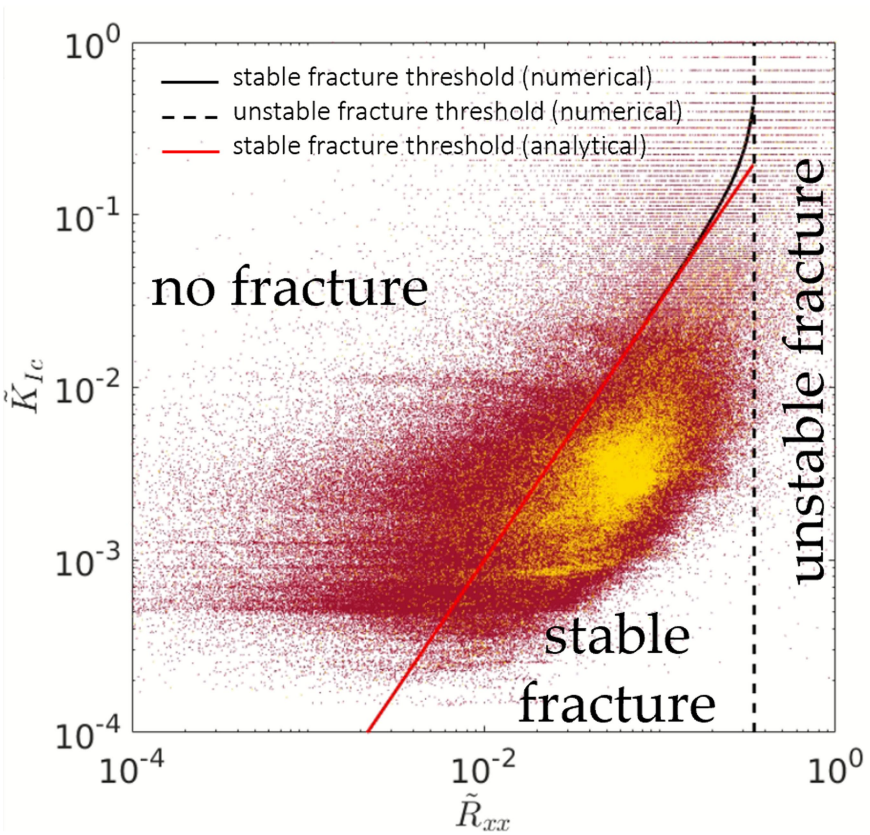

Extended Data Fig. 7 | Surface fracture stability diagram. The two parameters determining fracture stability, $\tilde{K}_{Ic}$ and $\tilde{R}_{xx}$, were computed at every 1 km × 1 km location on all ice shelves marked as red (n = 1,258,908 points) and all fracture features detected by the DCNN marked as yellow dots (n = 31,962). The frequency distribution of the yellow points is shown in Fig. 3c.

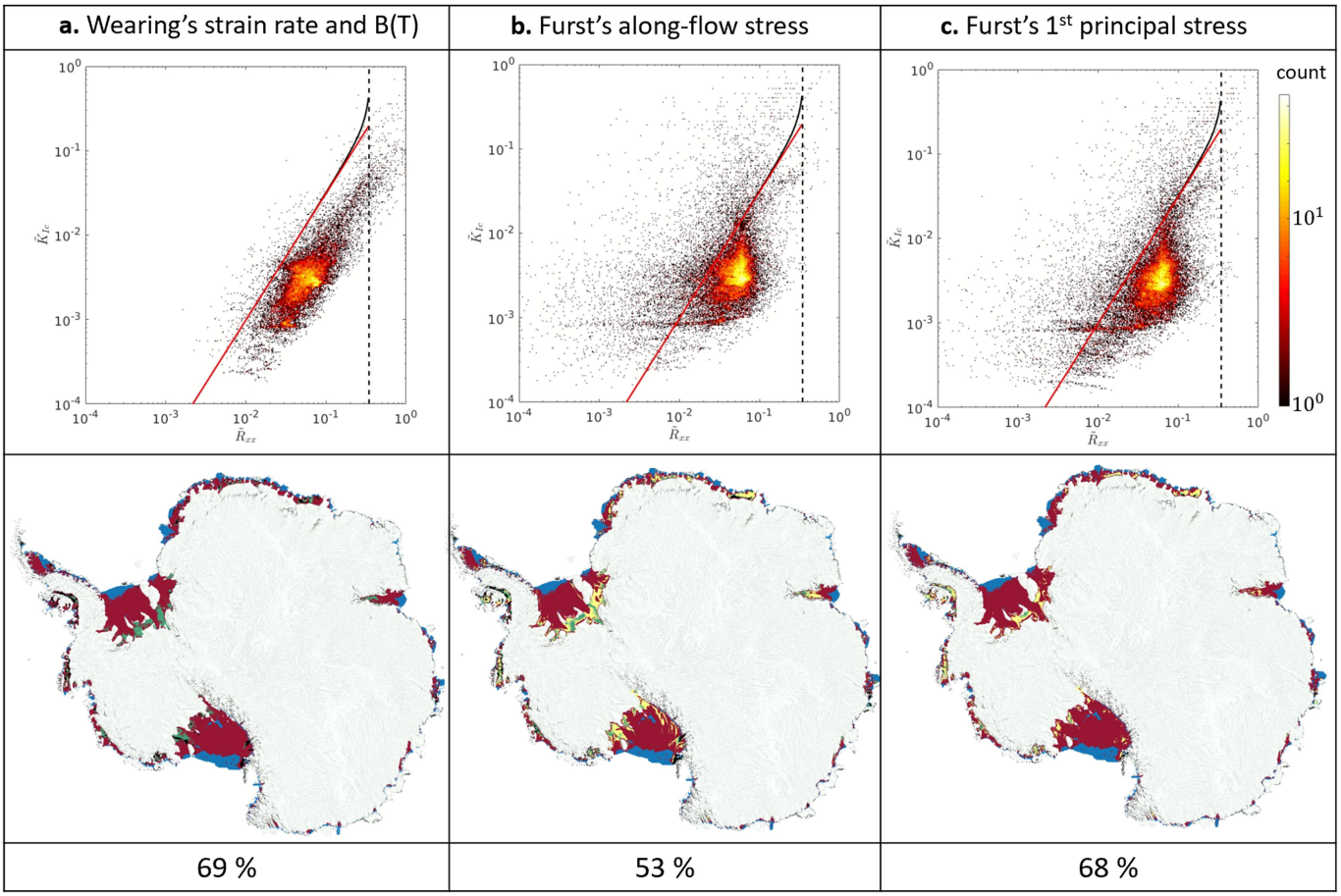

Extended Data Fig. 8 | Alternative stress computations. Sensitivity of surface fracture stability diagram (top) and the vulnerability map (bottom) to choices of stress and strain rate data. **a**–**c**, Results computed using strain rates calculated by ref. [61] (**a**) and ref. [13] along-flow stress (**b**) and first principal stress (**c**), which includes damage-induced ice softening. The colour scale for the bottom row is the same as Fig. 4. The percentage values in the bottom row denote the percentage of the total ice-shelf area that is in the red regime in the second row (that is, both buttressed and vulnerable to hydrofracture). Our main conclusions—that ice-shelf stresses closely agree with the fracture criteria, and that large buttressed areas are vulnerable to hydrofracture—are not affected by the use of these alternative stress fields.

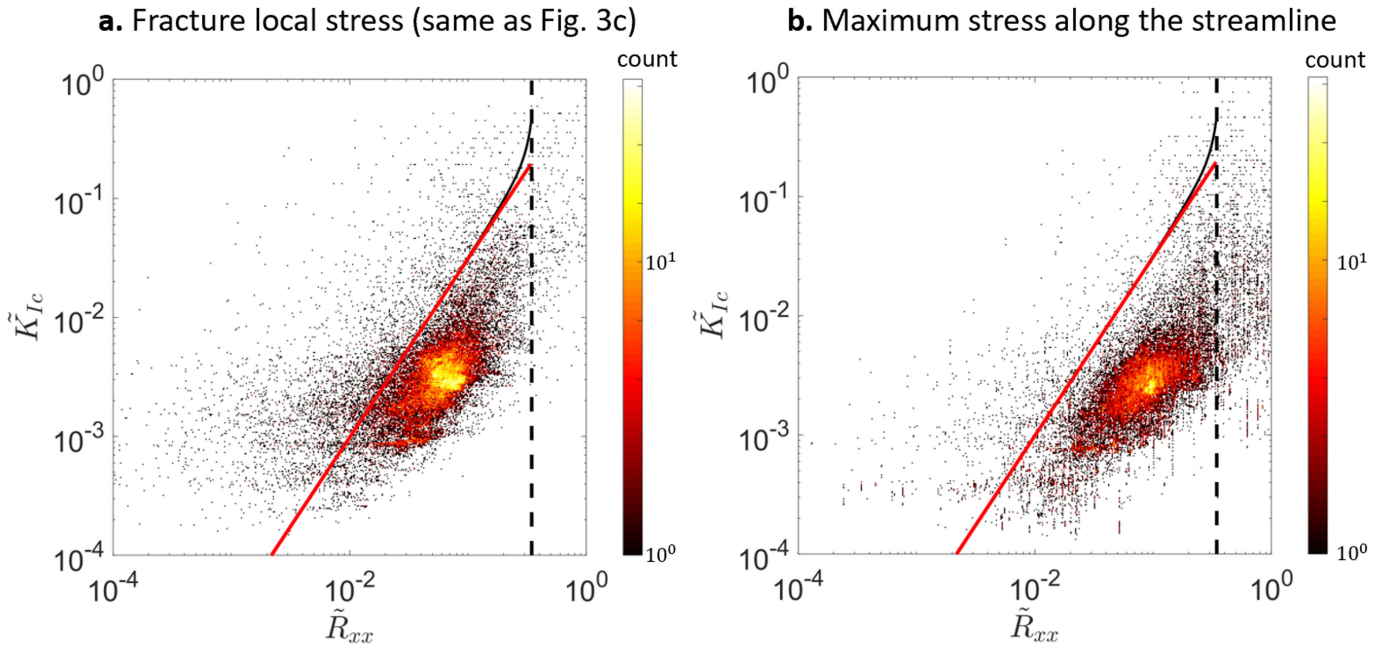

Extended Data Fig. 9 | Advection of fracture and stress history. We tracked the resistive stress upstream along streamlines (assuming steady-state) and identified the maximum dimensionless stress $\tilde{R}_{xx\max}$ each fracture feature had experienced in the past. **a**, The dimensionless parameters $\tilde{R}_{xx}$ and $\tilde{K}_{Ic}$ evaluated directly at the locations of fracture features are shown (same as Fig. 3c) for comparison. **b**, For each location identified as a fracture by the DCNN, we evaluated $\tilde{R}_{xx\max}$ and the corresponding $\tilde{K}_{Ic}$ at the location where $\tilde{R}_{xx\max}$ occurred. $\tilde{R}_{xx\max}$ calculated for most fractures features exceeds the threshold for surface fracture formation (red line; equation (2)).

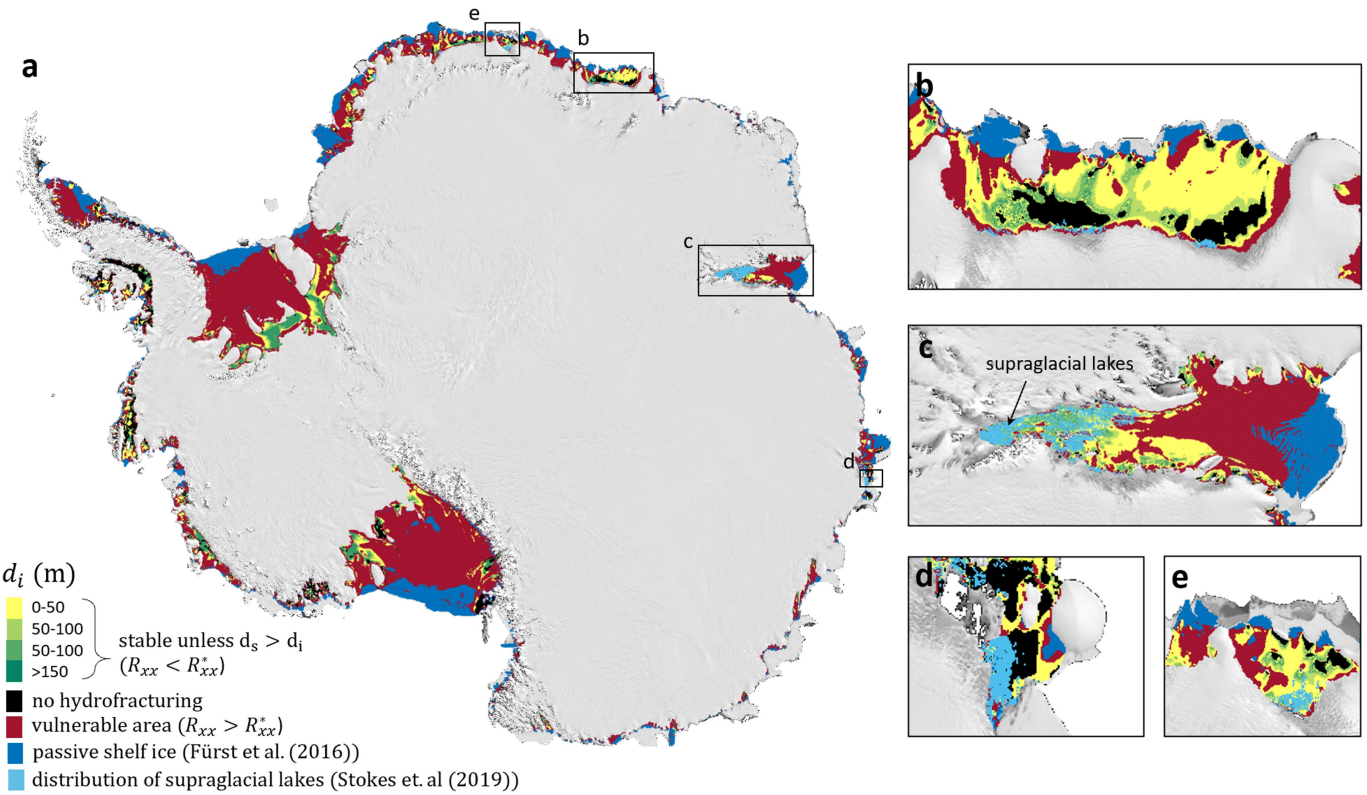

Extended Data Fig. 10 | East Antarctic lake locations compared with vulnerability map. Stokes et al.[25] have mapped lakes across much of East Antarctica for one melt season (2017), enabling us to compare these locations with our vulnerability map (Fig. 4). **a**–**e**, The lakes mapped by Stokes et al. are marked in light blue with expanded views shown in **b**–**e**. We find that only a tiny proportion of the ice-shelf area in East Antarctica accumulates meltwater, provides buttressing and is vulnerable to hydrofracture. An upper estimate of the overlap between lake-covered area (top circle of Fig. 1) and stress state-related vulnerable area (bottom left circle of Fig. 1) is only ~0.63% of the East Antarctic ice-shelf area.